IEEE Access
Multidisciplinary ⋮ Rapid Review ⋮ Open Access Journal

Received 8 August 2022, accepted 17 August 2022, date of publication 25 August 2022, date of current version 1 September 2022.

Digital Object Identifier 10.1109/ACCESS.2022.3201650

RESEARCH ARTICLE

Comparative Study of Two Degree-of-Freedom Rotary-Linear Machines With Permanent-Magnet Mover for High Dynamic Performance

YAOJIE HE, (Graduate Student Member, IEEE), SHUN CAI, (Member, IEEE), YOU ZHOU, (Member, IEEE), AND CHRISTOPHER H. T. LEE, (Senior Member, IEEE)
School of Electrical and Electronic Engineering, Nanyang Technological University, Singapore 639798

Corresponding author: Christopher H. T. Lee (chtlee@ntu.edu.sg)

This work was supported by the Ministry of Education (MOE), Singapore, under its MOE Academic Research Fund (AcRF) Tier 1 Program under Grant 2019-T1-002-064.

ABSTRACT This paper analyzes and evaluates various topologies of yokeless rotary-linear (RL) machine with permanent-magnet (PM) mover targeting for the achieving high dynamic performance. For the conventional yokeless RL machines, the single-stator topology features limited slot area for armature winding excited for both motions, and the coupled magnetic fields of both motions requires complex control strategy. In order to mitigate these issues, a double-stator RL machine with hybrid PMs array, which adopts the PMs with six magnetization directions, is proposed in this paper. An improved PMs array is introduced for the double-stator topology to achieve decoupled control for both motions. In addition, an analytical model of the radial flux density is derived to reveal the characteristics of the magnetic fields in different topologies. The parametric studies towards key dimensions are conducted to provide design guidelines and obtain the optimal design. Finally, the electromagnetic performances of the proposed design are compared systematically with the conventional single-stator counterparts. It is revealed that the proposed topology can enhance the performances in both motions, namely rotary and linear motions.

INDEX TERMS Two degree-of freedom machine, rotary-linear machine, robotic application, permanent-magnet machine, yokeless machine.

NOMENCLATURE

F_s	Airgap PM magnetomotive force (MMF)
v	Linear speed
ω	Rotary speed
x_0	Initial linear position
θ_0	Initial rotary position
τ_{sl}	Axial stator pole pitch
$\tau_{s\theta}$	Circumferential stator pole pitch
τ_{ml}	Axial mover pole pitch
$\tau_{m\theta}$	Circumferential mover pole pitch
l_{sp}	Axial stator pole length
w_{sp}	Circumferential stator pole width
P_0	Stator yoke permeance
P_1	Stator pole permeance
p_{ml}	Axial mover pole-pair number
$p_{m\theta}$	Circumferential mover pole-pair number
q_{sl}	Axial stator pole-pair number
$q_{s\theta}$	Circumferential stator pole-pair number

The associate editor coordinating the review of this manuscript and approving it for publication was Amin Mahmoudi.

I. INTRODUCTION

Nowadays, two degree-of-freedom (2DOF) rotary-linear (RL) system, which can achieve rotary motion and linear motion simultaneously and individually, has been investigated and utilized for the application such as robotic components, drilling tools [1], and injection machine [2]. The conventional RL system is presented in Fig. 1 [3]. The parallel coupled system and the series coupled system install two electric machines to form a double-machine system. To be specific, one electric machine is for rotary motion and the other is for linear motion. Such system requires additional mechanical structures, e.g., connector, housing, and fixture, to connect the two electric machines.

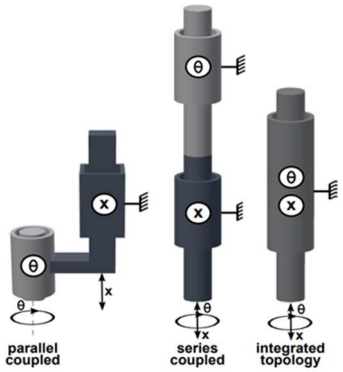

FIGURE 1. Topologies of conventional 2DOF RL system [3].

Consequently, extra space is required to accommodate actuators and mechanical connections, and the efficiency of the conventional RL system is inevitable deteriorated due to friction and sliding. Unlike the double-machine system, the integrated topology utilizes only one electric machine to achieve both rotary and linear motions. Upon the implementation of this integrated machine concept, a more compact design can be obtained.

Traditionally, the first RL machine was investigated in [4], which is a decoupled-flux RL machine. In this type of RL machine, the magnetic field of linear motion and rotary motion are isolated. In such case, the effective flux for each motion is decoupled by the corresponding stator. The machine structure combines the conventional rotary and linear machine along axial [5], [6], [7], circumferential [8], [9] or radial direction [10], [11], [12]. Thus, the performance of two motions, namely rotary and linear motions, can be analyzed and optimized separately in two-dimensional (2D) model [13], [14], which is time-saving for machine design. Additionally, the performances of the linear and rotary motion of the decoupled-flux RL machine are similar to the rotary and linear machine with the same structure. In order to avoid flux coupling issue, certain large gaps between the magnetic fields of two motions should be adopted, where the flux coupling effect has been investigated in [15] and [16]. Thus, the machine volume is relatively bulky, and the space utilization rate is deteriorated. Hence, this group of RL machines is not suitable for compact design.

If the magnetic fields of two motions are coexist in the same space, the RL machine can be referred as the coupled flux type [4]. In this type of RL machine, the space utilization is improved, and a more compact structure can be achieved. The PMs array can be classified as surface-mounted type [17], [18], spoke-type [19] and Halbach type [20]. In addition, some improvements towards these RL machines have been investigated such as PM utilization enhancement [21] and detent force suppression [22]. With the adoption of spoke-type PMs, the linear force and rotary torque are enhanced.

The linear acceleration and rotary acceleration are two essential dynamic performances for the RL machines targeting at servo applications (e.g., robotic arm) [23], [24], which are strongly related to the force-mass ratio and torque-inertia ratio. In other words, even though the force and torque are enhanced by adopting the spoke-type and Halbach PMs arrays, the linear and rotary accelerations may still be deteriorated due to the increased mass and inertia of the mover. Consequently, the improvement towards the dynamic performance may not be as significant as that towards the linear force and rotary torque. Besides, the fluxes of both motions are coupled in the same winding, the linear force and rotary torque (i.e., the helical motion) are declined than under single motion and a complex decoupling control scheme is required [25]. Meanwhile, a complex decoupling strategy is required in control side to achieve 2DOF control.

To solve the aforementioned problems, a new 2DOF RL machine with double-stator hybrid PMs array structure is proposed in this paper. Different from the traditional double-stator topologies in decoupled-flux RL machine, the magnetic fields of two motions are coupled in the mover side. Hence, the yokeless mover can be utilized to enhance the accelerations of the proposed machine. Meanwhile, the magnetic fields of two motions are decoupled by the mechanical salient stators. Thus, the linear and rotary motions can be controlled individually by the winding in each stator. In this paper, the magnetic fields of the proposed double-stator topology are theoretically modelled and analyzed. In addition, the parametric analysis of the proposed machine is conducted to provide the design guidelines for the RL machines with PMs mover structure. Finally, the electromagnetic performances of the RL machines with PM mover are compared systematically.

II. TOPOGOLIES OF RL MACHINES WITH PM MOVER

In this section, the topologies of various RL machines with PM movers are presented, and their corresponding airgap magnetic fields are analyzed. Since the PMs array in the proposed machine (i.e., with double-stator structure) is different from the single-stator counterpart, the design procedure and considerations will be investigated in detail. In this paper, the combination of pole pair numbers of PMs array and stator in axial and circumferential are chose as 5-pole-pair to 6-slot and 10-pole-pair to 12-slot respectively.

A. SINGLE-STATOR TOPOLOGIES

In Fig. 2, the topologies and PMs arrays of surface-mounted PM RL machine (termed as surface-mounted type), spoke-type PM RL machine (termed as spoke-type), and the Halbach PMs RL machine (termed as Halbach-type) are included for comparison. The spoke-type PMs bricks are presented in the squares with arrows, which are the magnetization directions. The radially magnetized PMs are the squares with crosses and dots. In the spoke-type, the black square means the iron brick. It should be mentioned that in the surface-mounted type, the back iron is replaced by the 3D printed fixture (i.e., presented in golden region). This structure can be used to reduce the mass and inertia of the

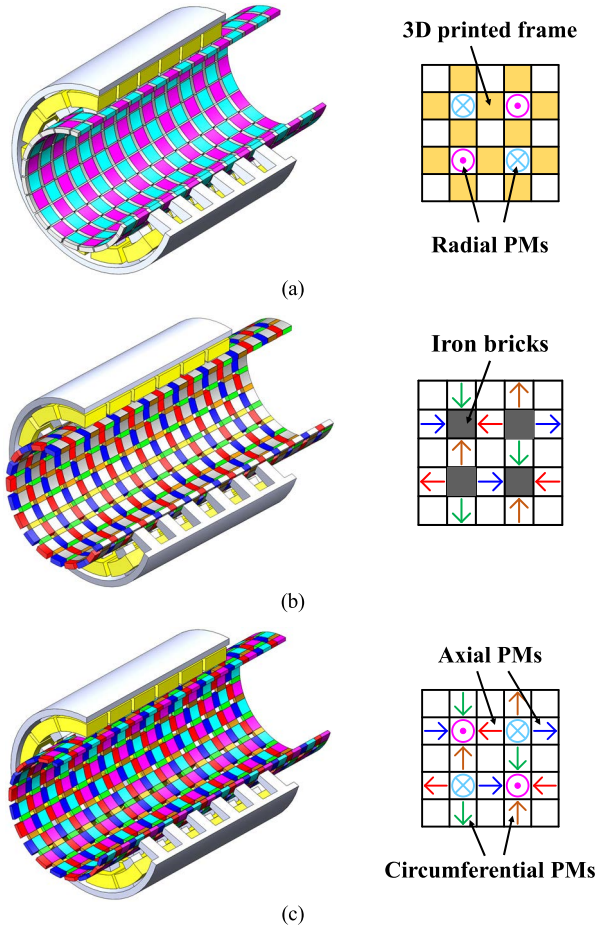

FIGURE 2. Topologies of conventional single-stator RL machines. (a) Surfaced-mounted PMs (i.e., surface-mounted type). (b) Spoke-type PMs (i.e., spoke type). (c) Halbach PMs array (i.e., Halbach type).

mover, hence providing higher accelerations [26]. The radial flux density in the airgap magnetic field by one unit of PMs array in the single-stator topologies is presented in Fig.3. It can be seen the magnetic field is alternating in both axial and circumferential directions.

B. DOUBLE-STATOR TOPOLOGIES

In the single-stator topologies, each coil is wound through two adjacent slots, which are in axial and circumferential directions. Thus, the current applied in each coil is limited by the smaller slot, and hence restricting the electromagnetic performances. In the proposed double-stator RL machine, two stators are mechanically salient along either axial or circumferential direction. It means the current of each motion is determined by the slot area in the corresponding stator. Consequently, the winding utilization rate is enhanced.

Another feature of the proposed machine is that the magnetic field in each airgap should be salient in only one direction. Taking the linear stator as an example, the stator pole is consistent along the circumferential direction. In such case, the integration of the airgap flux density varying along the circumferential direction is zero, which means the flux

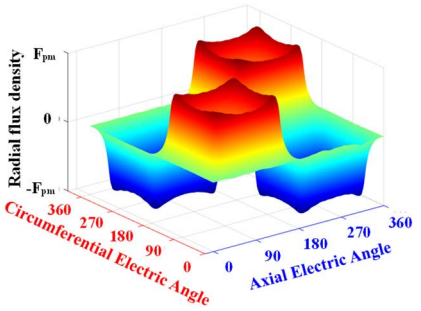

FIGURE 3. PM radial flux density in the single-stator topology.

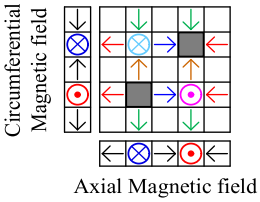

FIGURE 4. Formation of the double-stator PMs array.

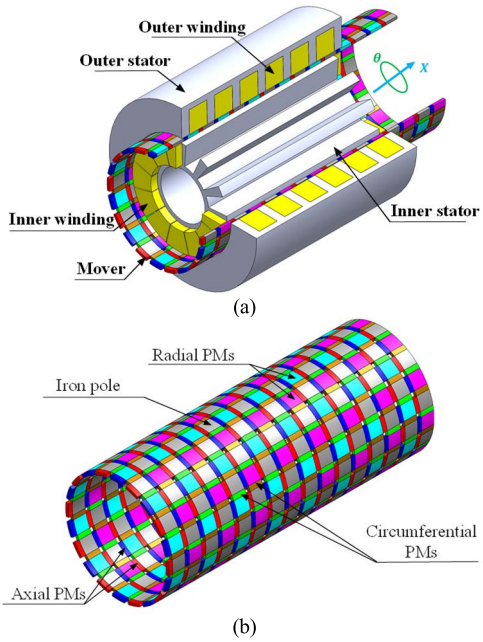

FIGURE 5. Topologies of the proposed machine. (a) Assembled structure. (b) PM Mover.

generated by this magnetic field is not coupled by the toroidal coil. A similar situation can be inferred in the rotary stator.

Fig. 4 presents the required magnetic fields and the PMs array. The meaning of each square is the same as that in Fig. 2. The PMs array is superimposed when the magnetic fields of the linear motion and rotary motion are arranged in the outer and inner, respectively.

For the PMs brick, the magnetization direction is consistent in both inner and outer airgaps. When the top right

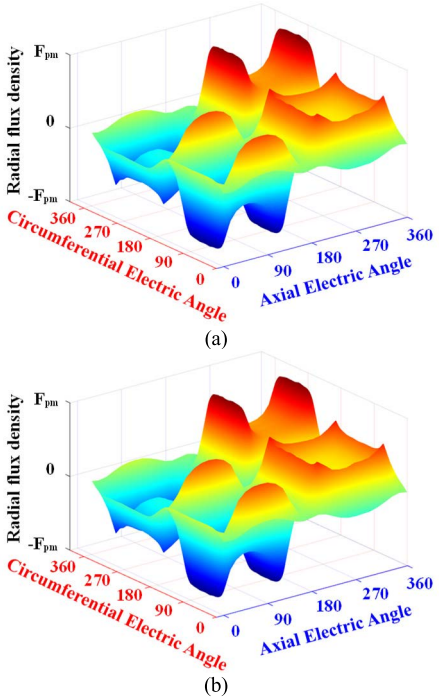

FIGURE 6. Radial flux density components in two airgaps. (a) Outer airgap. (b) Inner airgap.

region and bottom left region are considered, the radial flux density directions in two airgaps are the same. Thus, the radially magnetized PMs with opposite polarizations can be adopted in these two places. On the contrary, when an iron brick is adjacent with four spoke-type PMs, the magnetic polarizations in two airgaps are opposite. Hence, the requirement of top left and bottom right regions can be implemented. By selecting the magnetization direction of the spoke-type PMs, the polarization of the iron brick can be controlled.

Consequently, the PMs array for the double-stator topology can be formed and the structure of the proposed machine is presented in Fig. 5. The radial flux density of the designed PMs array in the outer and inner airgaps are illustrated and verified in Fig. 6.

The outer stator, which is similar to the stator of the tubular linear machine. The toroidal winding is selected to be applied as the outer winding. For limiting the length of the end winding, the concentrated winding is applied to the inner stator. Since the rotary motion exhibits higher electric frequency than the linear motion, the number of turns in of the inner winding is set lower than that in the outer winding, which equalizes the amplitudes of back-EMFs of two motions in each coil.

C. MAGNETIC FIELD ANALYSIS

In this section, the magnetic fields of the single-stator topology and the double-stator topology are modelled. The coupling effect of the radial flux density under two motions is analyzed for each topology.

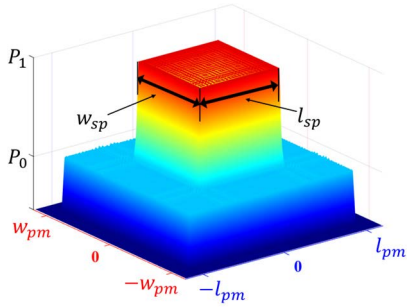

FIGURE 7. Stator airgap permeance in the single-stator topologies.

According to Fig. 3, the airgap magnetomotive force (MMF) generated by the PMs array in the single-stator topologies can be regarded as the square wave, varying with the axial position x and circumferential position θ. The Fourier series of such pattern can be expressed as:

$$\begin{cases} F_{PM,s}(x,\theta,t) \\ \quad = \sum_{n_{ml},n_{m\theta}=1}^{\infty} \begin{cases} D_{ml,m\theta,s} \sin\left[\dfrac{n_{ml}\pi\,(x-vt-x_0)}{\tau_{ml}}\right] \\ \sin\left[\dfrac{n_{m\theta}\pi\,(\theta-\omega t-\theta_0)}{\tau_{m\theta}}\right] \end{cases} \\ D_{ml,m\theta,s} \\ \quad = \begin{cases} \dfrac{16F_s}{n_{ml}n_{m\theta}\pi^2} \sin\left(\dfrac{n_{ml}\pi}{2}\right) \sin\left(\dfrac{n_{m\theta}\pi}{2}\right) \\ \sin\left(\dfrac{n_{ml}\pi l_r}{2\tau_{ml}}\right) \sin\left(\dfrac{n_{m\theta}\pi w_r}{2\tau_{m\theta}}\right) \end{cases} \end{cases} \tag{1}$$

The airgap permeance of the stator can be derived from a similar pattern in Fig. 7 with its Fourier series as:

$$\begin{cases} P_{s,s}(x,\theta) = P_{00,s} + \sum_{m_{sl}=1}^{\infty} P_{sl,0,s} \cos\left(\dfrac{2m_{sl}\pi x}{\tau_{sl}}\right) \\ \quad + \sum_{m_{s\theta}=1}^{\infty} P_{s\theta,0,s} \cos\left(\dfrac{2m_{s\theta}\pi\theta}{\tau_{s\theta}}\right) \\ \quad + \sum_{m_{sl},m_{s\theta}=1}^{\infty} P_{sl,s\theta,s} \cos\left(\dfrac{2m_{sl}\pi x}{\tau_{sl}}\right) \cos\left(\dfrac{2m_{s\theta}\pi\theta}{\tau_{s\theta}}\right) \end{cases} \tag{2}$$

the Fourier coefficients are:

$$\begin{cases} P_{00,s} = P_0 + (P_1 - P_0)\dfrac{l_{sp}w_{sp}}{\tau_{sl}\tau_{s\theta}} \\ P_{sl,0,s} = \dfrac{2(P_1-P_0)w_{sp}}{m_{sl}\pi\tau_{s\theta}} \sin\left(\dfrac{m_{sl}\pi l_{sp}}{\tau_{sl}}\right) \\ P_{s\theta,0,s} = \dfrac{2(P_1-P_0)l_{sp}}{m_{s\theta}\pi\tau_{sl}} \sin\left(\dfrac{m_{s\theta}\pi w_{sp}}{\tau_{s\theta}}\right) \\ P_{sl,s\theta,s} = \dfrac{4(P_1-P_0)}{m_{sl}m_{s\theta}\pi^2} \sin\left(\dfrac{m_{sl}\pi l_{sp}}{\tau_{sl}}\right) \sin\left(\dfrac{m_{s\theta}\pi w_{sp}}{\tau_{s\theta}}\right) \end{cases} \tag{3}$$

p_{ml}, $p_{m\theta}$, q_{sl} and $q_{s\theta}$ can be applied for analyzing the pole-pair numbers of the airgap magnetic field, which are:

$$\begin{cases} \tau_{ml} = \dfrac{l_e}{2p_{ml}} & \tau_{m\theta} = \dfrac{\pi}{p_{m\theta}} \\ \tau_{sl} = \dfrac{l_e}{q_{sl}} & \tau_{s\theta} = \dfrac{2\pi}{q_{s\theta}} \end{cases} \tag{4}$$

where l_e is the effective length in axial direction.

The radial flux density of the single-stator topologies can be obtained by $F_{PM,s}(x,\theta,t)$ and $P_{s,s}(x,\theta)$, as:

$$\begin{aligned} &B_s(x,\theta,t) \\ &= \sum_{n_{ml},n_{m\theta}=1}^{\infty} \left\{ \begin{array}{l} D_{ml,m\theta,s} P_{00,s} \sin \\ \times \left[\dfrac{n_{ml} p_{ml} 2\pi\,(x - vt - x_0)}{l_e} \right] \\ \sin\left[n_{m\theta} p_{m\theta} \pi\,(\theta - \omega t - \theta_0)\right] \end{array} \right. \\ &+ \sum_{\substack{n_{ml},n_{m\theta}=1 \\ m_{sl}=1}}^{\infty} \left\{ \begin{array}{l} \dfrac{D_{ml,m\theta,s} P_{sl,0,s}}{2} (\sin\alpha_{sl1} + \sin\alpha_{sl2}) \\ \sin\left[n_{m\theta} p_{m\theta} \pi\,(\theta - \omega t - \theta_0)\right] \end{array} \right\} \\ &+ \sum_{\substack{n_{ml},n_{m\theta}=1 \\ m_{s\theta}=1}}^{\infty} \left\{ \begin{array}{l} \dfrac{D_{ml,m\theta,s} P_{s\theta,0,s}}{2} (\sin\alpha_{s\theta1} + \sin\alpha_{s\theta2}) \\ \sin\left[\dfrac{n_{ml} p_{ml} 2\pi\,(x - vt - x_0)}{l_e}\right] \end{array} \right\} \\ &+ \sum_{\substack{n_{ml},n_{m\theta}=1 \\ m_{sl},m_{s\theta}=1}}^{\infty} \left\{ \begin{array}{l} \dfrac{D_{ml,m\theta,s} P_{sl,s\theta,s}}{4} (\sin\alpha_{sl1} + \sin\alpha_{sl2}) \\ (\sin\alpha_{s\theta1} + \sin\alpha_{s\theta2}) \end{array} \right\} \end{aligned} \tag{5}$$

$$\begin{cases} \alpha_{sl1} = (n_{ml}p_{ml} + m_{sl}q_{sl}) \left[\dfrac{2\pi x}{l_e} - \dfrac{n_{ml}p_{ml}2\pi\,(vt + x_0)}{(n_{ml}p_{ml} + m_{sl}q_{sl})\,l_e} \right] \\ \alpha_{sl2} = (n_{ml}p_{ml} - m_{sl}q_{sl}) \left[\dfrac{2\pi x}{l_e} - \dfrac{n_{ml}p_{ml}2\pi\,(vt + x_0)}{(n_{ml}p_{ml} - m_{sl}q_{sl})\,l_e} \right] \\ \alpha_{s_\theta 1} = (n_{m\theta}p_{m\theta} + m_{s\theta}q_{s\theta}) \left[\theta - \dfrac{m_{p\theta}p_{m\theta}\,(\omega t + \theta_0)}{n_{m\theta}p_{m\theta} + m_{s\theta}q_{s\theta}} \right] \\ \alpha_{s_\theta 2} = (n_{m\theta}p_{m\theta} - m_{s\theta}q_{s\theta}) \left[\theta - \dfrac{m_{p\theta}p_{m\theta}\,(\omega t + \theta_0)}{n_{m\theta}p_{m\theta} - m_{s\theta}q_{s\theta}} \right] \end{cases} \tag{6}$$

The open-circuit radial flux density in the single-stator topologies consists of nine components. For each component, it is varying in both axial and circumferential directions. The pole-pair numbers in both directions of each component can be derived and listed in Table 1.

The initial pole-pair numbers of radial flux density in two motions are $n_{ml}p_{ml}$ and $n_{m\theta}p_{m\theta}$. Due to the adoption of salient stator, the pole-pair numbers change to $|n_{ml}p_{ml} \pm m_{sl}q_{sl}|$ and $|n_{m\theta}p_{m\theta} \pm m_{s\theta}q_{s\theta}|$. Besides, the modulated component of one motion is coupling with the initial and modulated components of the other motion. In Fig. 8, the spatial components of the radial flux density in single-stator topology are presented, which are derived from the optimal designs after the parametric study in Section III. It can be seen that the radial flux densities in both axial and circumferential direction are modulated.

Since the flux modulated effect is verified, the pole-pair numbers of the PMs array and the stator can be arranged according to the flux modulation theory [27], [28] to obtain a large gear ratio. Based on these design concepts, the linear force and rotary torque of the RL machine can be further improved [29].

TABLE 1. Characteristics of airgap radial flux density in the single-stator topologies.

No.	Linear pole pairs	Rotary pole pairs
1	$n_{ml}p_{ml}$	$n_{m\theta}p_{m\theta}$
2	$n_{ml}p_{ml} + m_{sl}q_{sl}$	$n_{m\theta}p_{m\theta}$
3	$\lvert n_{ml}p_{ml} - m_{sl}q_{sl}\rvert$	$n_{m\theta}p_{m\theta}$
4	$n_{ml}p_{ml}$	$n_{m\theta}p_{m\theta} + m_{s\theta}q_{s\theta}$
5	$n_{ml}p_{ml}$	$\lvert n_{m\theta}p_{m\theta} - m_{s\theta}q_{s\theta}\rvert$
6	$n_{ml}p_{ml} + m_{sl}q_{sl}$	$n_{m\theta}p_{m\theta} + m_{s\theta}q_{s\theta}$
7	$n_{ml}p_{ml} + m_{sl}q_{sl}$	$\lvert n_{m\theta}p_{m\theta} - m_{s\theta}q_{s\theta}\rvert$
8	$\lvert n_{ml}p_{ml} - m_{sl}q_{sl}\rvert$	$n_{m\theta}p_{m\theta} + m_{s\theta}q_{s\theta}$
9	$\lvert n_{ml}p_{ml} - m_{sl}q_{sl}\rvert$	$\lvert n_{m\theta}p_{m\theta} - m_{s\theta}q_{s\theta}\rvert$

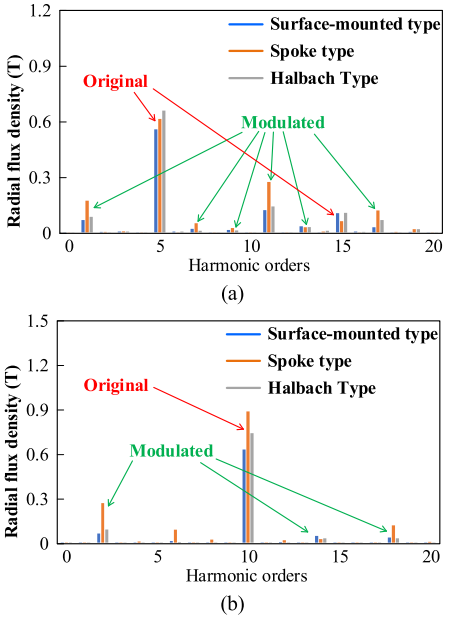

FIGURE 8. Spatial components of radial flux density in single-stator topologies (a) Along axial direction. (b) Along circumferential direction.

Another characteristic of the single-stator RL machine is that the open-circuit radial flux density in each position is varying along both axial and circumferential directions at the same time. For example, the amplitude of coil flux linkage under linear motion is varying with the position of the coil along circumferential direction. Likewise, the amplitude of coil flux linkage under rotary motion is defined by its axial position. The coil back-EMF can be expressed as:

$$\begin{aligned} E_{c,s} = E_{m,s} &\cos\left[\frac{2\pi\,(p_{ml}vt + x_0)}{l_e} + \gamma_l\right] \\ &\times \cos\left(p_{m\theta}\omega t + \varphi_0 + \gamma_\theta\right) \end{aligned} \tag{7}$$

where γ_l and γ_ϑ are denoted as the electric angle of the initial position of the coil in linear motion and rotary motion, respectively.

In the double-stator topology, as shown in Fig. 6, the MMF patterns generated by the PMs array are different in two airgaps. The stators in the double-stator topology are mechanically salient in only one direction. Thus, the MMF and permeance models are different in the double-stator topology. The Fourier series of the airgap MMF pattern model in the outer airgap are presented as:

$$\begin{cases} F_{PM,do}(x,\theta,t) = \sum\limits_{n_{ml}=1}^{\infty} B_{ml,0,do} \sin \\ \quad \times \left[\dfrac{n_{ml}\pi\ (x - vt - x_0)}{\tau_{ml}}\right] \\ \quad + \sum\limits_{n_{ml},m_{m\theta}=1}^{\infty} \left\{ \begin{array}{l} C_{ml,m\theta,do} \sin \left[\dfrac{n_{ml}\pi\ (x - vt - x_0)}{\tau_{ml}}\right] \\ \cos \left[\dfrac{m_{m\theta}\pi\ (\theta - \omega t - \theta_0)}{\tau_{m\theta}}\right] \end{array} \right\} \\ B_{ml,0,do} = \dfrac{4Fw_r}{n_{ml}\pi} \sin\left(\dfrac{n_{ml}\pi}{2}\right) \sin\left(\dfrac{n_{ml}\pi l_r}{2\tau_{ml}}\right) \\ C_{ml,m\theta,do} = \left[\begin{array}{l} \dfrac{16F}{n_{ml}m_{m\theta}\pi^2} \sin\left(\dfrac{n_{ml}\pi}{2}\right) \cos\left(\dfrac{m_{m\theta}\pi}{2}\right) \\ \sin\left(\dfrac{n_{ml}\pi l_r}{2\tau_{ml}}\right) \sin\left(\dfrac{m_{m\theta}\pi w_r}{2\tau_{m\theta}}\right) \end{array} \right] \end{cases} \tag{8}$$

The outer stator permeance model can be expressed as:

$$\begin{cases} P_{s,do}(x) = P_{00,do} + \sum\limits_{m_{sl}=1}^{\infty} P_{sl,0,do} \cos\left(\dfrac{2m_{sl}\pi x}{\tau_{sl}}\right) \\ P_{00,do} = P_0 + (P_1 - P_0)\dfrac{l_{sp}}{\tau_{sl}} \\ P_{sl,0,do} = \dfrac{2\,(P_1 - P_0)}{m_{sl}\pi} \sin\left(\dfrac{m_{sl}\pi l_{sp}}{\tau_{sl}}\right) \end{cases} \tag{9}$$

Likewise, the Fourier series of the airgap MMF pattern and the permeance models in the inner airgap can be expressed as:

$$\begin{cases} F_{PM,di}(x,\theta,t) = \sum\limits_{n_{m\theta}=1}^{\infty} D_{0,m\theta,di} \sin \\ \quad \times \left[\dfrac{n_{m\theta}\pi\ (\theta - \omega t - \theta_0)}{\tau_{m\theta}}\right] \\ \quad + \sum\limits_{m_{ml},n_{m\theta}=1}^{\infty} \left\{ \begin{array}{l} C_{ml,m\theta,di} \cos \left[\dfrac{m_{ml}\pi\ (x - vt - x_0)}{\tau_{ml}}\right] \\ \sin \left[\dfrac{n_{m\theta}\pi\ (\theta - \omega t - \theta_0)}{\tau_{m\theta}}\right] \end{array} \right\} \\ D_{0,m\theta,di} = \dfrac{4Fl_r}{n_{m\theta}\pi} \sin\left(\dfrac{n_{m\theta}\pi}{2}\right) \sin\left(\dfrac{n_{m\theta}\pi w_r}{2\tau_{m\theta}}\right) \\ C_{ml,m\theta,di} = \left\{ \begin{array}{l} \dfrac{16F}{m_{ml}n_{m\theta}\pi^2} \cos\left(\dfrac{m_{ml}\pi}{2}\right) \sin\left(\dfrac{n_{m\theta}\pi}{2}\right) \\ \sin\left(\dfrac{m_{ml}\pi l_r}{2\tau_{ml}}\right) \sin\left(\dfrac{n_{m\theta}\pi w_r}{2\tau_{m\theta}}\right) \end{array} \right\} \end{cases} \tag{10}$$

The inner stator permeance model can be expressed as:

$$\begin{cases} P_{s,di}(\theta) = P_{00,di} + \sum\limits_{m_{s\theta}=1}^{\infty} P_{0,s\theta,di} \cos\left(\dfrac{2m_{s\theta}\pi\theta}{\tau_{s\theta}}\right) \\ P_{00,di} = P_0 + (P_1 - P_0)\dfrac{w_{sp}}{\tau_{s\theta}} \\ P_{0,s\theta,di} = \dfrac{2\,(P_1 - P_0)}{m_{s\theta}\pi} \sin\left(\dfrac{m_{s\theta}\pi w_{sp}}{\tau_{s\theta}}\right) \end{cases} \tag{11}$$

Similar to the single-stator topology, the radial flux density component of the double-stator topology in outer airgap can be derived by multiplying $F_{PM,do}(x,\theta,t)$ and $P_{s,do}(x)$, which can be expressed as:

$$\begin{aligned} &B_{do}(\theta,x,t) \\ &= \sum_{n_{ml}=1}^{\infty} B_{0,ml,do}P_{00,do} \\ &\quad \times \sin\left[\frac{2n_{ml}p_{ml}\pi\ (x - vt - x_0)}{l_e}\right] \\ &\quad + \sum_{n_{ml},m_{m\theta}=1}^{\infty} \left\{ \begin{array}{l} C_{ml,m\theta,do}P_{00,do} \sin \\ \times \left[\dfrac{2n_{ml}p_{ml}\pi\ (x - vt - x_0)}{l_e}\right] \\ \cos\left[m_{m\theta}p_{m\theta}\ (\theta - \omega t - \theta_0)\right] \end{array} \right\} \\ &\quad + \sum_{\substack{n_{ml}=1 \\ m_{sl}=1}}^{\infty} \frac{B_{0,ml,do}P_{sl,0,do}}{2} (\sin\alpha_{sl1} + \sin\alpha_{sl2}) \\ &\quad + \sum_{\substack{n_{ml},m_{m\theta}=1 \\ m_{sl}=1}}^{\infty} \left\{ \begin{array}{l} \dfrac{C_{ml,m\theta,do}P_{sl,0,do}}{2} (\sin\alpha_{sl1} + \sin\alpha_{sl2}) \\ \cos\left[m_{m\theta}p_{m\theta}\ (\theta - \omega t - \theta_0)\right] \end{array} \right\} \end{aligned} \tag{12}$$

Likewise, the radial flux density in inner airgap is:

$$\begin{aligned} &B_{di}(\theta,x,t) \\ &= \sum_{n_{m\theta}=1}^{\infty} D_{0,m\theta,di}P_{00,di} \sin\left[n_{m\theta}p_{m\theta}\ (\theta - \omega t - \theta_0)\right] \\ &\quad + \sum_{m_{ml},n_{m\theta}=1}^{\infty} \left\{ \begin{array}{l} B_{ml,m\theta,di}P_{00,di} \cos \\ \times \left[\dfrac{2m_{ml}p_{ml}\pi\ (x - vt - x_0)}{l_e}\right] \\ \sin\left[n_{m\theta}p_{m\theta}\ (\theta - \omega t - \theta_0)\right] \end{array} \right\} \\ &\quad + \sum_{\substack{n_{m\theta}=1 \\ m_{s\theta}=1}}^{\infty} \frac{D_{0,m\theta,di}P_{0,s\theta,di}}{2} (\sin\alpha_{s\theta1} + \sin\alpha_{s\theta2}) \\ &\quad + \sum_{\substack{m_{ml},n_{m\theta}=1 \\ m_{s\theta}=1}}^{\infty} \left\{ \begin{array}{l} \dfrac{B_{ml,m\theta,di}P_{0,s\theta,di}}{2} (\sin\alpha_{s\theta1} + \sin\alpha_{s\theta2}) \\ \cos\left[\dfrac{2m_{ml}p_{ml}\pi\ (x - vt - x_0)}{l_e}\right] \end{array} \right\} \end{aligned} \tag{13}$$

In $F_{PM,do}$ and $F_{PM,di}$, the components varying among both x and θ, are magnetically salient along the same direction. These components can be modulated and coupled by the corresponding winding as analyzed in Section B.

TABLE 2. Key parameters in RL machine with mover PMs structure.

Index	Value
Stator outer radius R_{so} (mm)	60
Axial stator length l_s (mm)	120
Stator yoke height h_{sy} (mm)	4
Axial mover pole pitch τ_{ml} (mm)	12
Airgap length g (mm)	0.6
Central radius of the mover R_m (mm)	37.5
Mover thickness h_m (mm)	3
Axial central brick length l_r (mm)	6-11.5
Circumferential central brick width w_r (degree)	12-17.5
Axial stator pole ratio γ_l	0.8-1.2
Circumferential stator pole ratio γ_w	0.8-1.2

For the permeance models in two airgaps, they can be obtained from the permeance pattern in conventional rotary and linear machine, which are in 2D forms. Besides, the permeance model $P_{s,do}$ and $P_{s,di}$ can be derived from (2) and (3) by assuming $w_{sp} = 2\tau_{s\theta}$ and $l_{sp} = 2\tau_{sl}$. It should be noted that the permeance model in the double-stator topology is a special form of that in the single-stator topologies. In this special form, the coefficient of the component which is varying in only either x or θ is increased. Meanwhile, the coefficients of the other components are declined to zero.

In B_{do} and B_{di}, the spatial harmonics varying along both x and θ still exist. However, since both stators show single-direction saliency, the working flux coupled by the winding in each stator is varying along with the corresponding stator. In addition, since the amplitude of the coupled components and the stator poles is enlarged in the double-stator topology, the amplitude of the effective flux is higher than that in the single-stator topologies.

III. INFLUENCE OF DESIGN PARAMETERS

In this section, the effect of the dimensions of the central brick (i.e., the region of the iron brick or radial PMs) and the stator pole arc/length ratio towards linear force and rotary torque are presented and analyzed. These parameters are essential for determining the coefficients in the radial flux density models and the output performances, as presented in the last section. The fixed parameters and the variation ranges of the targeted parameters are listed in Table 2 and illustrated in Fig. 9. The axial stator pole ratio γ_l and circumferential stator pole ratio γ_w are defined as:

$$r_l = \frac{l_{sp}}{l_r} \tag{14}$$

$$r_w = \frac{w_{sp}}{w_r} \tag{15}$$

In each study, only two parameters are changed, and the other parameters are kept constant. The mover thickness significantly affects not only the linear force and rotary torque, but also the accelerations of both motions. Hence, the study towards mover thickness is presented in the following section.

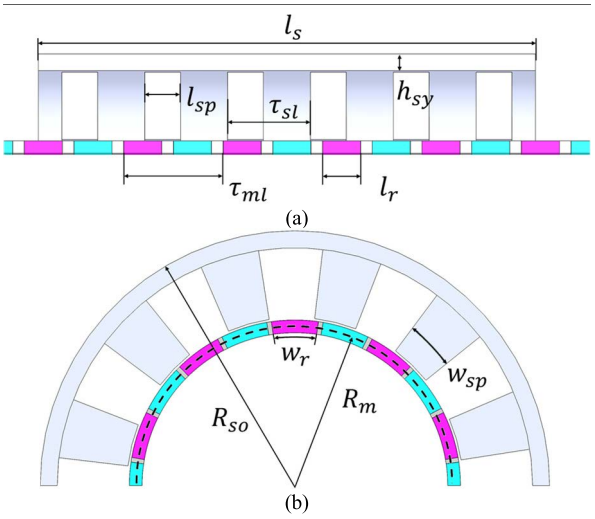

FIGURE 9. Key parameters for RL machines with PMs mover structure.

A. DIMENSIONS OF THE CENTRAL BRICK

With larger l_r and w_r, the space utilization of mover is higher because the area of the air region is shrunk. However, it leads to thin spoke-type PMs, which might deteriorate performance on linear force and rotary torque. Since the mass and inertia are increased, the accelerations in both motions are compromised. On the contrary, if the l_r and w_r are smaller, the thicker spoke-type PMs can be obtained which might be beneficial for enhancing the performance of the RL machines. However, it results with increased leakage flux so as the shrunk of the permeance of the mover side. Hence, these two parameters should be investigated in detail.

Because the optimal designs of all four topologies might be in large difference, the optimal regions of l_r and w_r are determined for each topology within the fixed parameter range at first stage. Afterwards, the performances towards the average force and average torque for each topology in its optimal region are obtained, as presented in Fig. 10 and Fig. 11, respectively. With the consideration of the force ripple and torque ripple, the optimal l_r and w_r can be obtained.

Without the adoption of spoke-type PMs, the optimal ranges of l_r and w_r in the surface-mounted type is larger than that in the other topologies. Meanwhile, both the linear force and rotary torque in the surface-mounted type are the smallest among all structures. The main reason is that the permeance of the mover side is small. As shown in Fig. 12, the flux is flowing in PMs and air that exhibits smaller permeability than iron material. On the other hand, due to the yokeless structure, the flux needs to flow in the inner air region, which enhances the length of the flux path. Thus, the effective flux in surface-mounted type is much smaller than other topologies.

In spoke type, the spoke-type PMs are adopted, with the radially magnetized PMs replaced by the iron poles. Compared with surface-mounted type, the permeance of the mover in spoke type is increased since the permeability of the iron material is larger than that of the air and PMs. Consequently,

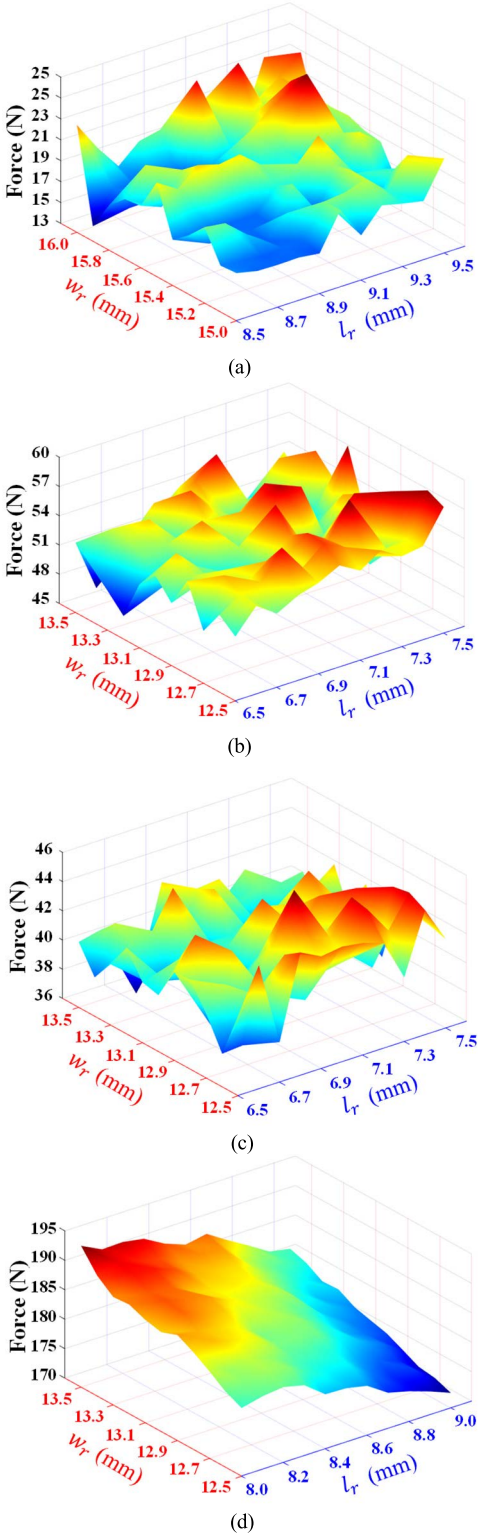

FIGURE 10. Linear force variation with l_r and w_r in (a) Surface-mounted type. (b) Spoke type. (c) Halbach type. (d) Proposed design.

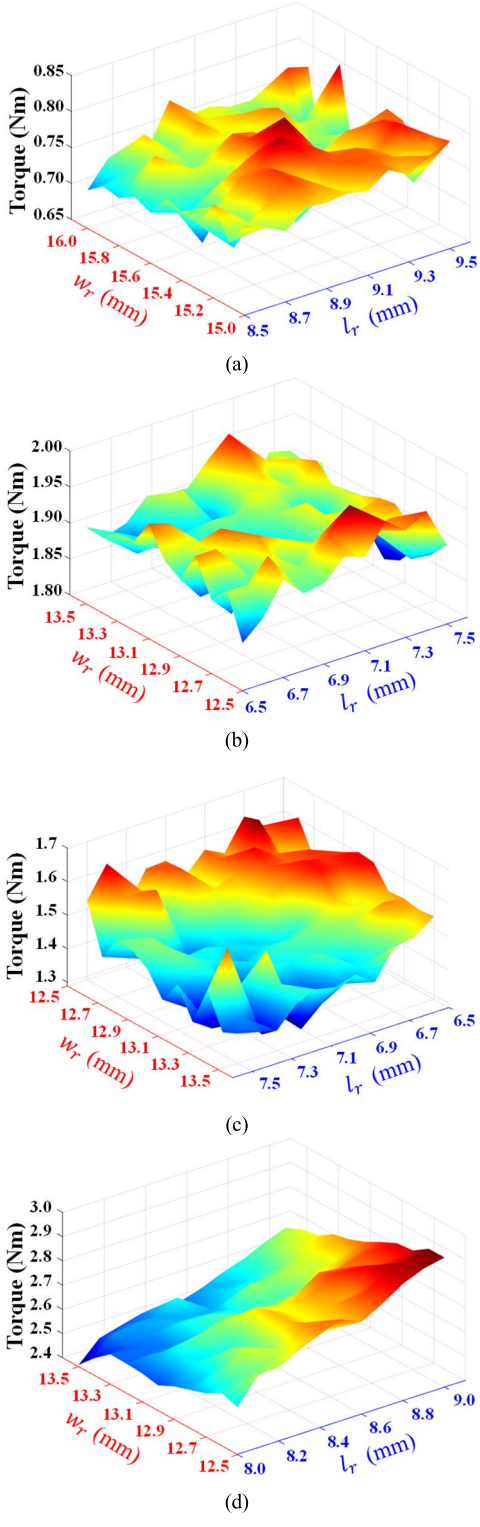

FIGURE 11. Rotary torque variation with l_r and w_r in (a) Surface-mounted type. (b) Spoke type. (c) Halbach type. (d) Proposed design.

the linear force and rotary torque are enhanced, and the PMs utilization rate is increased. The optimal ranges of l_r and w_r in spoke type is smaller than that in surface-mounted type since the circumferentially and axially magnetized PMs need to be thicker.

In Halbach type, the iron poles sandwiched by the spoke-type PMs are replaced by radial magnetized PMs. Thus, a Halbach PMs array is formed that strengthens the magnetic field in the airgap. Different from the surface-mounted type, when the flux path in the mover side is considered, the flux

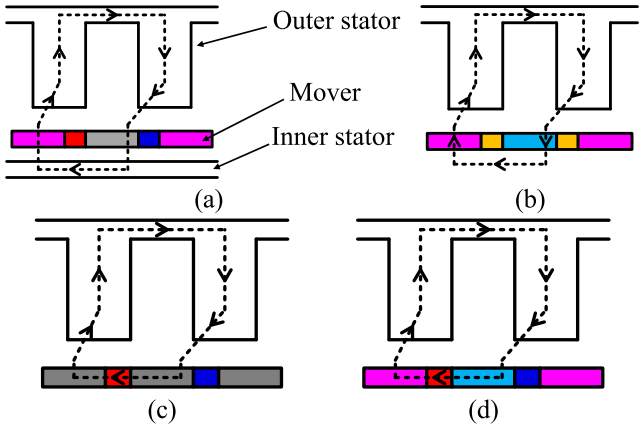

FIGURE 12. Airgap axial flux path in (a) Proposed design. (b) Surface-mounted type. (c) Spoke type. (d) Halbach type.

flows from the north pole to the south pole inside of PM bricks rather than through the air region beneath the mover. In such case, the length of the flux path is reduced, and hence the permeance of the flux path is increased. Compared with spoke type, the optimal ranges of l_r and w_r are the same, which means the force and torque performances are highly contributed by the spoke-type PMs. However, despite the fact that the MMF is enhanced by adopting radially magnetized PMs, the permeability of the PMs is much smaller than that in the iron poles. Consequently, the linear force and rotary torque are less than those in spoke type but still larger than that in surface-mounted type.

In the proposed design, when l_r is decreased while w_r is increased, a larger value of linear force can be obtained. On the contrary, the rotary torque is enhanced with larger l_r and smaller w_r. For the linear motion, the smaller l_r means the thicker axially magnetized spoke-type PMs. As analyzed in previous section, the spoke-type PMs contains higher impact on the average force than that of the surface-mounted PMs. Hence, it significantly changes the optimal region of l_r and w_r. Meanwhile, with larger w_r, the thickness of the circumferentially magnetized PMs is reduced. Thus, the effective circumferential length of the linear unit, which is similar to the stack length in the linear machine, is increased. Consequently, if small l_r and large w_r are set, the linear force would be increased. Likewise, the effect of the variation of l_r and w_r towards rotary torque can be explained by the similar reason.

The fitness function is utilized to transfer multiple-objective optimization into single-objective optimization by assigning weight value to each objective. Generally, the function can be expressed as:

$$c_i = \sum_{j=1}^{m} w_j \frac{x_{j,i}}{x_{j,\max}} + \sum_{k=1}^{n} w_k \frac{x_{k,\min}}{x_{k,i}} \tag{16}$$

where c_i is the fitness value of design i. $x_{j,max}$ and $x_{k,min}$ represent the maximum and minimum value of the objective j and k among all designs. $x_{j,i}$ and $x_{k,i}$ are the value of objective j and k in design i, respectively. Particularly, w_j and w_k are the weighting coefficient of objective j and k, which satisfy:

$$\sum_{j=1}^{m} w_j + \sum_{k=1}^{n} w_k = 1 \tag{17}$$

It should be noted that some objectives should be maximized (e.g., linear force and rotary torque) while others should be minimized (e.g., force ripple and torque ripple). Hence, the objectives are divided into two groups, and the numbers of objectives in two groups are denoted as m and n, respectively.

In the fitness function, the objectives are calculated in per-unit value, which balances the contribution of each objective towards the fitness value of one design. Finally, the fitness values in the optimal regions of all topologies are calculated and presented in Fig. 13. Consequently, the optimal l_r and w_r can be obtained for further analysis.

B. STATOR POLE LENGTH / ARC

In the double-stator topology, the outer stator pole length and inner stator pole arc independently affect the electric loading of two motions. However, for the single-stator topologies, the electric loadings of two motions are affected by these two parameters simultaneously. For example, if the slot along the circumferential direction is kept smaller than that along the axial direction, the current is fixed when adjusting the axial stator pole ratio since the current is defined by the smaller slot under constant current density. In such case, the slot area in two directions, as affected the stator pole length and stator pole arc, should be optimized synchronously.

Apart from balancing the electric loading and the magnetic loading, r_l and r_w also defines the effective length of the structure for single motion. For example, with larger r_l, the length of the stator pole is larger. It means the effective ''stack length'' for rotary motion is enlarged. If the axial slot is still larger than the circumferential slot, the current is determined by the circumferential slot, i.e., so it is constant under this situation. As a result, a higher rotary torque can be obtained. However, if r_l is too large, the axial slot will be smaller than the circumferential slot. Hence, the current is determined by the axial slot area, which is decreased with larger r_l. As a result, the rotary torque is decreased. The characteristic of linear force and r_w can be analyzed similarly.

The results of the parametric study towards the dimensions in single-stator topologies are presented in Fig. 14. It can be seen the spoke type exhibits the highest level in both linear force and rotary torque, following by Halbach type, i.e., both of them are higher than the surface- mounted type. For all three single-stator topologies, the maximum values of linear force and rotary torque are obtained when r_l and r_w below than 1. Furthermore, the optimal values of r_l and r_w in each topology balance the slot areas in two directions, which means the current calculated by two slot areas are close to each other.

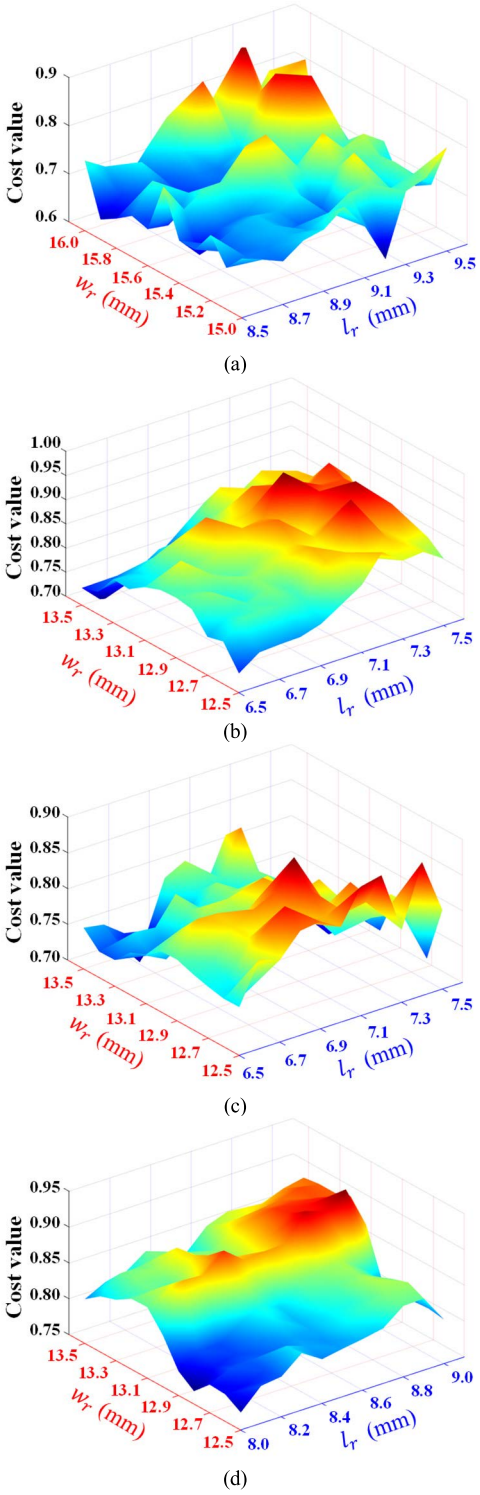

FIGURE 13. Fitness value of the parametric study towards l_r and w_r in (a) Surface-mounted type. (b) Spoke type. (c) Halbach type. (d) Proposed design.

In the double-stator topology, since the windings and magnetic fields of two motions are decoupled, the linear and rotary performances are greatly depending on r_l and r_w, respectively. However, the dimensions of two types of stator poles together affect the permeance P_1 in (7) and (9). This is

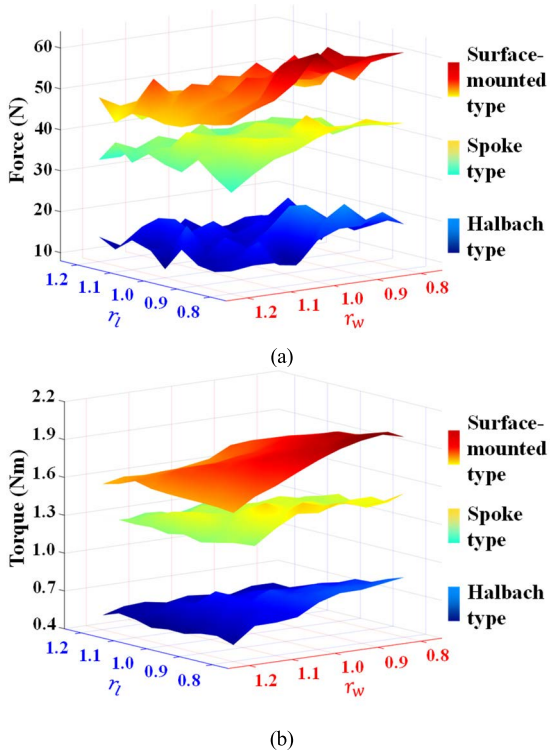

FIGURE 14. Linear and rotary performances varying with r_l and r_w of the single-stator topologies. (a) Linear force (b) Rotary torque.

because the flux of each motion flows through the mover and both stators. As shown in Fig. 12(a), the flux of linear motion starts from the mover PMs array and travels through the linear stator and flows back to the mover side. Next, instead of going through inside of the mover, the flux flows through the rotary stator and gets back to its starting point. Since the rotary stator is slotless along the axial direction, it works as a back-iron and contains no modulation effect on linear flux. However, the inner stator pole ratio r_w affects the permeance of flux path in the rotary stator. Consequently, it contains the influence towards the linear flux. Likewise, the linear stator pole ratio r_l affect the rotary flux in the same manner.

The results of linear and rotary performances varying with r_l and r_w in the double-stator topology are illustrated in Fig. 15. With smaller r_l, a higher linear force can be obtained. Meanwhile, a higher torque can be achieved with smaller r_w. The obtained result is similar to that in the single-stator topology. Besides, the linear force and rotary torque are fluctuating with both r_w and r_l respectively, and hence verifying the suggested concepts above.

From Fig. 15 (c) and (d), the local minimum values of force ripple and torque ripple can be achieved, and the optimal values for r_l and r_w are obtained. It can be seen the force ripple and torque ripple are very large. One of the reasons is that the hybrid PMs array brings additional mechanical pole-slot structure. Different from the 2D magnetic field Fourier series, (6) and (8) exhibit some components varying with both x and θ, which increase the detent force and cogging torque of the proposed machine.

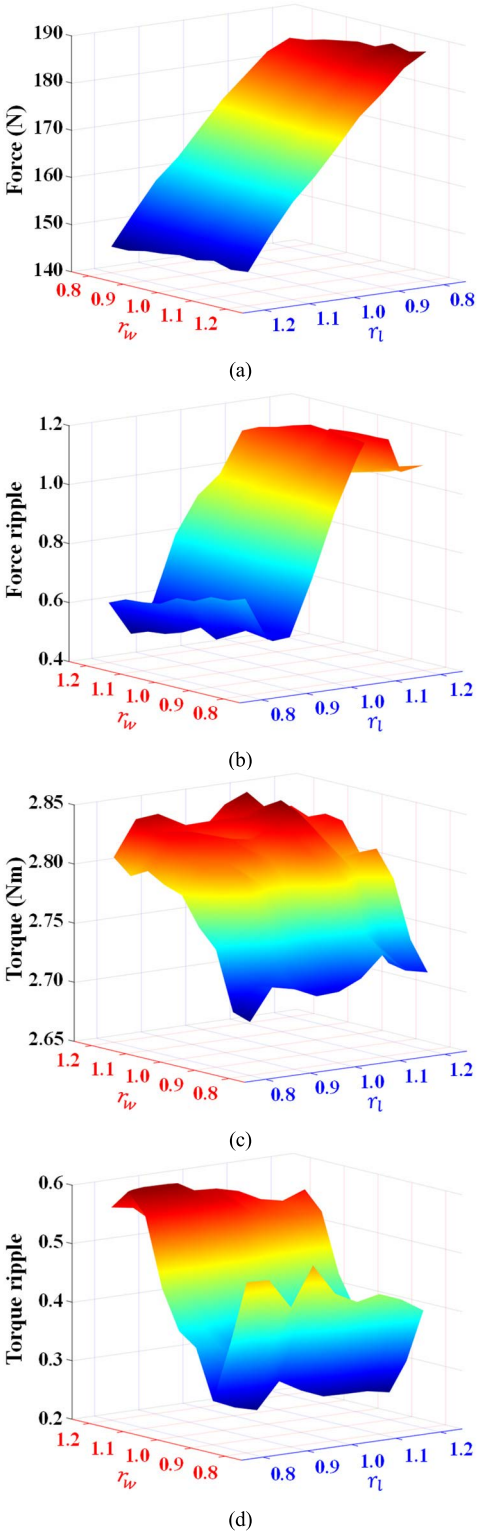

FIGURE 15. Linear and rotary performances varying with r_l and r_w of the double-stator topology. (a) Linear force (b) Rotary torque (c) Force ripple (d) Torque ripple.

IV. COMPARISON OF THE OPTIMAL DESIGNS

After the magnetic field analysis and parametric study, the optimized design for each topology can be obtained for further comparison. As mentioned above, the accelerations of both motions are essential indexes for evaluating the RL machine applied in robotic application. For fair comparison, the linear stroke, named as the linear motion range, and the radius of the centerline of the mover are fixed.

It should be noted the thickness of the mover significantly affect the linear force, rotary torque, the mass and inertia of the mover. Consequently, the accelerations are largely depending on the mover thickness. For the single-stator topologies, with thicker mover, higher MMF is generated by the PMs and the larger radius of the airgap is obtained since the central radius of the mover is fixed. As a result, the magnetic loading is enlarged. However, the electric loading is sacrificed because the slot area is reduced. In the double-stator topology, since the linear part is set outside, the impact of the mover thickness to linear motion is similar to that in the single-stator topologies. However, for the rotary part, the slot area and, the radius of the inner airgap are both decreased.

In Fig. 16, the results of linear force, linear accelerations, rotary torque, and rotary accelerations varying with the mover thickness are presented. For the linear performance, while the linear force increases along with the thicker mover, the linear acceleration is decreased. Among the single stator topologies, for every mover thickness, spoke type exhibits the highest force and acceleration. Also, Halbach type is better than Type1 in these two indexes. In addition, the proposed machine exhibits much higher value in both linear force and linear acceleration than the other three single-stator topologies.

As for rotary performance, the double-stator topology exhibits smaller rotary torque and rotary accelerations when the mover thickness getting large. One of the reasons is that the heat dissipation condition of the inner stator is worse than that of the outer stator. Hence, the current density applied in the inner winding is considered to be lower than that in outer winding. The phase MMF generated by winding in the inner stator (474A) is less than that in the outer stator (885A). However, in the single stator topologies, the coil MMF is fixed in two motions due to the shared winding. In general, it can be seen that with thicker mover, a higher force and torque can be obtained while the accelerations of both motions are deteriorated. In such case, the mover thickness should be selected based on application requirement.

The performance summary of all topologies is listed in Table 3. The outer radiuses of all topologies are fixed while the effective axial length in the double-stator topology is longer than that in the single-stator topologies. This is because the outer stator adopts auxiliary pole for mitigating the end effect in linear motion. Thus, the effective length in the double-stator topology is one stator pole length longer than that in the single-stator topologies.

Among the single-stator topologies, spoke type exhibits the highest linear force and force density. However, since it adopts thicker mover than Halbach type, the linear acceleration is weakened. Even in the surface-mounted type, while the linear force is 31% less than spoke type, the linear acceleration is nearly the same. this is because that the mass of the mover in surface-mounted type is 32% less than that in

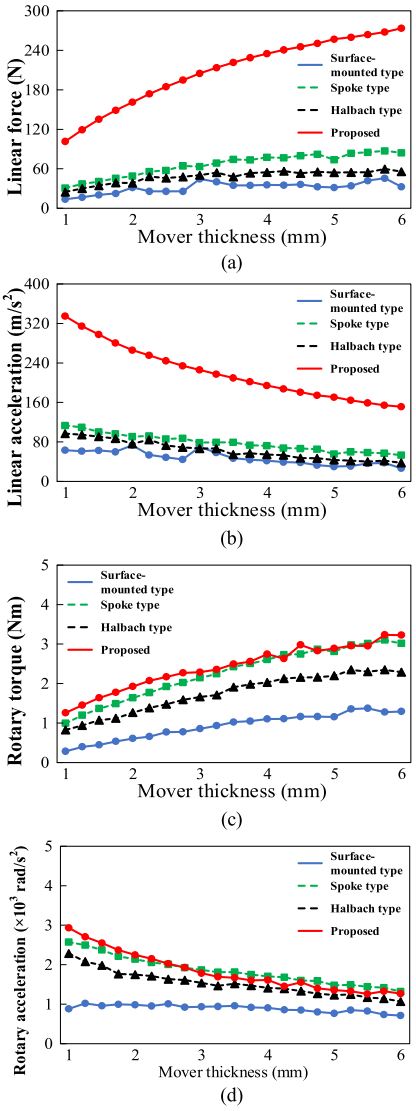

FIGURE 16. Performances comparison of all machines varying with the mover thickness (a) Linear force. (b) Rotary torque. (c) Linear acceleration. (d) Rotary acceleration.

spoke type due to the 3D printed frame. To take high force density and linear acceleration into consideration, spoke type and Halbach type are the improved topology compared with surface-mounted type. However, when considering the rotary performance, spoke type exhibits 127% and 51% higher torque than the other two single-stator topologies. In such case, even with the highest mass and inertia, the rotary acceleration in spoke type is only 8% less than that in Halbach type. Moreover, the power factors in spoke type are the highest among the single-stator topologies under both linear motion and rotary motion. The main reason behind this enhancement may come from the most effective flux modulation effect, as presented in Fig. 8.

Due to the thickest mover, the mass and inertia of the proposed machine exhibit the largest values among all

TABLE 3. Performances of all topologies.

Index	Surface-mounted type	Spoke type	Halbach type	Proposed
Stator outer radius (mm)		60		
Total volume ($\times 10^{-6}$ m^3)		1357.17		1443.69
Total PM volume ($\times 10^{-6}$ m^3)	41.48	28.27	39.17	59.73
Mover thickness (mm)	3	3	2.25	4
Linear mover pole pitch (mm)		12		
Linear stator pole pitch (mm)		10		
Linear stroke (mm)		72		
Linear speed (m/s)		1.2		
Linear force (N)	45.80	66.23	47.58	228.19
Mover mass (kg)	0.71	1.04	0.63	1.22
Linear acceleration (m/s^2)	64.87	63.68	75.52	187.04
Force density (kN/m^3)	33.75	48.80	35.06	158.06
Linear copper loss (W)	19.98	24.76	26.23	19.97
Linear power factor	0.87	0.92	0.91	0.89
Rotary mover pole pair		10		
Rotary slot number		12		
Rotary speed (rad/s)		1800		
Rotary torque (Nm)	0.92	2.09	1.38	2.80
Mover inertia (kg·mm^2)	990	1460	880	1710
Rotary acceleration (rad/s^2)	929.29	1431.50	1568.18	1637.42
Torque density (kNm/m^3)	0.68	1.54	1.02	1.94
Rotary copper loss (W)	19.98	24.76	26.23	6.53
Rotary power factor	0.91	0.93	0.92	0.91

topologies. Even with the largest mass and inertia, the proposed machine still produces the largest linear force and linear acceleration within the pool, i.e., 245% and 148% higher than the largest values in the single-stator topologies. Meanwhile, it can be seen that the proposed machine exhibits the smallest copper loss, which results the linear heat efficiency of the proposed concept is 327% higher than that of single-stator topology.

For the rotary performance, the proposed machine can provide 34% higher rotary torque and 4.4% higher rotary acceleration than the single-stator topologies. Since the phase MMF in the inner winding is lower than that of the outer winding, the copper loss of the inner winding is much lower than that of single-stator topologies. Consequently, the rotary heat efficiency of the proposed machine is 598% higher than single-stator topologies. In conclusion, the proposed machine can largely enhance the performances in both motions.

V. MECHANICS OF THE PROPOSED CONCEPT

Since the proposed machine consists of dual-sided stator and the yokeless mover, proper mechanical structure design needs to be taken into consideration. One potential form for the mechanical assembling for the proposed machine is illustrated as Fig. 17. Besides the main electromagnetic part of the proposed machine, one inner shaft, three bearings, one output shaft with end cap and one housing are arranged. The inner shaft (i.e., black part) is used to locate the inner stator and providing the space for connecting the inner winding. The output shaft with end cap (i.e., green part) locates the mover and output the linear force and rotary torque. The housing is used to fix the outer stator. In order to transmit both linear and

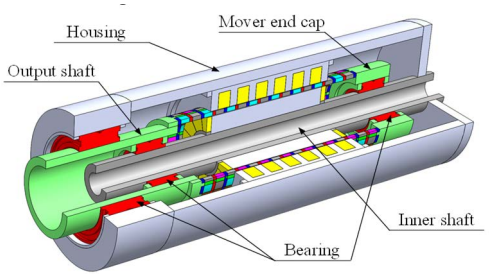

FIGURE 17. Mechanical assembling of the proposed machine.

rotary motions, the bearings are chosen as the combined bearing. In robotic applications, since the linear stroke is limited, the bending effect of the inner shaft can be withstood. The sleeve or carbon fiber material can be also considered for the mover for fixing the PMs and iron brick.

In the proposed machine, natural cooling is considered to be utilized in both outer and inner stators. The current density of the outer stator armature winding is set as 5A/mm^2. It should be noted, it is difficult to transfer the heat generated by the inner stator armature winding to the outside space. Thus, the current density of this part is set 4A/mm^2 in the optimal performance comparison.

VI. CONCLUSION

In this paper, a comparative study of various yokeless RL machines is conducted. These machines are designed to meet the requirements in linear force density, rotary torque density, as well as accelerations of both motions for robotic applications. In the conventional single stator machine, the mover can be made up of surface-mounted, spoke-type or Halbach PMs array. Meanwhile, in the proposed double-stator machine, a hybrid PMs array is designed as the mover adopting the PMs with six magnetization directions and iron bricks. Through the analysis of the magnetic field model, the newly designed PMs array brings more harmonics in flux modulating effect, which enriches the amplitude of the working harmonics. Since the magnetic fields of two motions are decoupled, the conventional concentrated winding and toroidal winding can be adopted in the rotary and linear stator, respectively. With a better utilization of working harmonics, the proposed double-stator machine can produce much better electromagnetic performances, including linear force and rotary torque, than its single-stator conventional counterparts.

REFERENCES

[1] J. F. Pan, Y. Zou, and N. C. Cheung, "Performance analysis and decoupling control of an integrated rotary–linear machine with coupled magnetic paths," *IEEE Trans. Magn.*, vol. 50, no. 2, pp. 761–764, Feb. 2014.

[2] O. Safdarzadeh, A. Mahmoudi, E. Afjei, and H. Torkaman, "Rotary-linear switched reluctance motor: Analytical and finite-element modeling," *IEEE Trans. Magn.*, vol. 55, no. 5, pp. 1–10, May 2019.

[3] K. J. Meessen, "Electromagnetic fields and interactions in 3D cylindrical structures: Modeling and application," Ph.D. thesis, Dept. Elect. Eng., Eindhoven Univ. Technol., Eindhoven, The Netherlands, 2012.

[4] L. Xie, J. Si, Y. Hu, and Z. Wang, "Overview of 2-degree-of-freedom rotary-linear motors focusing on coupling effect," *IEEE Trans. Magn.*, vol. 55, no. 4, pp. 1–11, Apr. 2019.

[5] K. Guo and Y. Guo, "Optimization design of parallel double stator and outer mover linear rotary permanent magnet machine used for drilling robot," in *Proc. IEEE Int. Conf. Appl. Supercond. Electromagn. Devices (ASEMD)*, Oct. 2020, pp. 1–2.

[6] T. J. Teo, H. Zhu, S.-L. Chen, G. Yang, and C. K. Pang, "Principle and modeling of a novel moving coil linear-rotary electromagnetic actuator," *IEEE Trans. Ind. Electron.*, vol. 63, no. 11, pp. 6930–6940, Nov. 2016.

[7] M. M. Nezamabadi, E. Afjei, and H. Torkaman, "Design, dynamic electromagnetic analysis, FEM, and fabrication of a new switched-reluctance motor with hybrid motion," *IEEE Trans. Magn.*, vol. 52, no. 4, pp. 1–8, Apr. 2016.

[8] L. Xie, J. Si, Y. Hu, H. Feng, and K. Ni, "Characteristics analysis of the motions of the two-degree-of-freedom direct drive induction motor," *IEEE Trans. Ind. Electron.*, vol. 67, no. 2, pp. 931–941, Feb. 2020.

[9] P. Wang, W. Hua, W. Yu, C. Tang, G. Zhang, and R. Cao, "A novel two degrees-of-freedom rotary-linear flux-switching permanent magnet machine," in *Proc. 22nd Int. Conf. Electr. Mach. Syst. (ICEMS)*, Aug. 2019, pp. 1–5.

[10] G. Zhang, R. Nie, J. Si, C. Gan, and Y. Hu, "Optimal design of a novel double-stator linear-rotary flux-switching permanent-magnet generator for offshore wind-wave energy conversion," in *Proc. IEEE Energy Convers. Congr. Expo. (ECCE)*, Oct. 2021, pp. 4300–4305.

[11] S. Li, K. W. E. Cheng, N. Cheung, and Y. Zou, "Design and control of a decoupled rotary-linear switched reluctance motor," *IEEE Trans. Energy Convers.*, vol. 33, no. 3, pp. 1363–1371, Sep. 2018.

[12] S. Miric, R. Giuffrida, G. Rohner, D. Bortis, and J. W. Kolar, "Design and experimental analysis of a selfbearing double-stator linear-rotary actuator," in *Proc. IEEE Int. Electric Mach. Drives Conf. (IEMDC)*, May 2021, pp. 1–8.

[13] Y. He, H. Chen, and C. H. T. Lee, "Design of a decoupled double-stator flux-switching permanent-magnet rotary-linear motor with two degree-of-freedom motion," in *Proc. 47th Annu. Conf. IEEE Ind. Electron. Soc. (IECON)*, Oct. 2021, pp. 1–6.

[14] L. Xu, M. Lin, X. Fu, and N. Li, "Design and analysis of a double-stator linear-rotary permanent-magnet motor," *IEEE Trans. Appl. Supercond.*, vol. 26, no. 4, pp. 1–4, Jun. 2016.

[15] L. Xu, M. Lin, X. Fu, X. Zhu, C. Zhang, and W. Wu, "Orthogonal magnetic field analysis of a double-stator linear-rotary permanent magnet motor with orthogonally arrayed permanent magnets," *IEEE Trans. Magn.*, vol. 53, no. 11, pp. 1–4, Nov. 2017.

[16] L. Xie, J. Si, T.-F. Wu, Y. Hu, J. Zhou, and S. Xu, "Analysis and suppression techniques of helical motion coupling effect for the 2DoF direct drive induction machine," *IEEE Trans. Ind. Electron.*, vol. 69, no. 2, pp. 1200–1210, Feb. 2022.

[17] P. Jin, H. Lin, S. Fang, Y. Yuan, Y. Guo, and Z. Jia, "3-D analytical linear force and rotary torque analysis of linear and rotary permanent magnet actuator," *IEEE Trans. Magn.*, vol. 49, no. 7, pp. 3989–3992, Jul. 2013.

[18] G. Krebs, A. Tounzi, B. Pauwels, D. Willemot, and F. Piriou, "Modeling of a linear and rotary permanent magnet actuator," *IEEE Trans. Magn.*, vol. 44, no. 11, pp. 4357–4360, Nov. 2008.

[19] W. Kitagawa, M. Mori, and T. Takeshita, "Design and analysis of two-degree-of-freedom actuator using PMSM and LSM," in *Proc. IEEE 10th Int. Conf. Power Electron. Drive Syst. (PEDS)*, Apr. 2013, pp. 506–511.

[20] P. Jin, Y. Yuan, G. Jian, H. Lin, S. Fang, and H. Yang, "Static characteristics of novel air-cored linear and rotary Halbach permanent magnet actuator," *IEEE Trans. Magn.*, vol. 50, no. 2, pp. 977–980, Feb. 2014.

[21] K. Guo, S. Fang, H. Lin, H. Yang, Y. Guo, and P. Jin, "Optimization design and analysis of a linear-rotary permanent magnet actuator with interlaced poles," in *Proc. IEEE Vehicle Power Propuls. Conf. (VPPC)*, Oct. 2016, pp. 1–6.

[22] K. Guo, S. Fang, H. Lin, Y. Huang, Y. Zhang, and H. Yang, "A linear-rotary permanent magnet actuator with independent magnetic circuit structure," *IEEE Trans. Appl. Supercond.*, vol. 26, no. 7, pp. 1–6, Oct. 2016.

[23] K. J. Meessen, J. J. H. Paulides, and E. A. Lomonova, "Analysis and design considerations of a 2-DoF rotary-linear actuator," in *Proc. IEEE Int. Electric Mach. Drives Conf. (IEMDC)*, May 2011, pp. 336–341.

[24] T. T. Overboom, J. W. Jansen, E. A. Lomonova, and F. J. F. Tacken, "Design and optimization of a rotary actuator for a two-degree-of-freedom $z\phi$-module," *IEEE Trans. Ind. Appl.*, vol. 46, no. 6, pp. 2401–2409, Sep. 2010.

[25] P. Jin, H. Lin, S. Fang, and S. L. Ho, "Decoupling control of linear and rotary permanent magnet actuator using two-directional $d-q$ transformation," *IEEE Trans. Magn.*, vol. 48, no. 10, pp. 2585–2591, Oct. 2012.

[26] S. Miric, M. Schuck, A. Tuysuz, and J. W. Kolar, "Double stator linear-rotary actuator with a single set of mover magnets," in *Proc. IEEE Energy Convers. Congr. Expo. (ECCE)*, Sep. 2018, pp. 750–757.
[27] X. Zhu, C. H. T. Lee, C. C. Chan, L. Xu, and W. Zhao, "Overview of flux-modulation machines based on flux-modulation principle: Topology, theory, and development prospects," *IEEE Trans. Transport. Electrific.*, vol. 6, no. 2, pp. 612–624, Jun. 2020.
[28] H. Chen, A. M. EL-Refaie, Y. Zuo, S. Cai, S. Xie, and C. H. T. Lee, "Evaluation of a contra-rotating flux-modulated machine featured with dual flux-modulation for wind power generation," *IEEE Trans. Ind. Electron.*, vol. 69, no. 9, pp. 8770–8781, Sep. 2022.
[29] J. Zhu, Y. Zuo, H. Chen, J. Chen, and C. H. T. Lee, "Deep-investigated analytical modeling of a surface permanent magnet Vernier motor," *IEEE Trans. Ind. Electron.*, vol. 69, no. 12, pp. 12336–12347, Dec. 2022.

YAOJIE HE (Graduate Student Member, IEEE) received the B.Sc. degree in electrical engineering and automation from the College of Electrical and Information Engineering, Hunan University, Changsha, China, in 2018. He is currently pursuing the Ph.D. degree with the School of Electrical and Electronics Engineering, Nanyang Technology University, Singapore. His research interests include two degree-of-freedom (2DOF) electric machines, rotary-linear machines, and linear machines.

SHUN CAI (Member, IEEE) was born in Hubei, China. He received the B.Eng. and M.Sc. degrees in electrical engineering from Zhejiang University, Hangzhou, China, in 2014 and 2017, respectively, and the Ph.D. degree in electrical engineering from The University of Sheffield, Sheffield, U.K., in 2020.

Since 2021, he has been a Research Fellow with Nanyang Technological University, Singapore. His research interests include design and analysis of novel permanent magnet machines for automobile application and renewable power generation.

YOU ZHOU (Member, IEEE) was born in China, in 1993. He received the B.E.E. degree in electrical engineering from Chongqing University, Chongqing, China, in 2016, and the Ph.D. degree in electrical engineering from the Huazhong University of Science and Technology, Wuhan, China, in 2021.

Since 2021, he has been a Research Fellow with Nanyang Technological University, Singapore. His research interests include the design and analysis of the linear flux-modulation permanent-magnet machines and high-power/torque permanent-magnet machines.

CHRISTOPHER H. T. LEE (Senior Member, IEEE) received the B.Eng. (Hons.) and Ph.D. degrees in electrical engineering from the Department of Electrical and Electronic Engineering, The University of Hong Kong, Hong Kong.

He was a Postdoctoral Fellow and then a Visiting Assistant Professor at the Massachusetts Institute of Technology, USA. He currently works as an Assistant Professor at Nanyang Technological University, Singapore and an Honorary Assistant Professor at The University of Hong Kong. His research interests include electric machines and drives, renewable energies, and electromechanical propulsion technologies. In these areas, he has published one book, three books chapters, and over 120 refereed articles.

Dr. Lee has received many awards, including MDPI Energies Young Investigator Award, NRF Fellowship, Nanyang Assistant Professorship, Li Ka Shing Prize (the Best Ph.D. Thesis Prize), and Croucher Foundation Fellowship. He is an Associate Editor of the IEEE TRANSACTIONS ON INDUSTRIAL ELECTRONICS, IEEE TRANSACTIONS ON ENERGY CONVERSION, IEEE ACCESS, and *IET Renewable Power Generation*. He is a Chartered Engineer in Hong Kong.